ChemElectroChem

Research Article
doi.org/10.1002/celc.202400650

Chemistry Europe
European Chemical Societies Publishing

www.chemelectrochem.org

Balancing the Aggregation of Cobalt Phthalocyanine on Carbon Nanohorn for Efficient H_2O_2 electrosynthesis in Neutral Electrolyte

Yiqi Ding,[a] Zhuo Xing,*[b] Chunguang Kuai,[c] Feng Ryan Wang,*[c] and Yuzheng Guo*[a]

Oxygen reduction reaction (ORR) driven by renewable electricity in neutral electrolyte presents a promising way for generating H_2O_2, which is suitable for daily sanitation and hygiene management. Cobalt phthalocyanine (CoPc) serves as an effective molecular electrocatalyst, providing active sites to facilitate H_2O_2 generation during ORR through a uniform distribution on carbon supports. However, the catalytic performance currently falls short of industrial application requirements. Herein, we employed carbon nanohorns with abundant oxygen functional groups (CNH(O)) to support CoPc, thereby optimizing the distribution of CoPc and enhancing the generation of active sites with electron-deficient Co centres. Control experiments and characterizations demonstrate the electron-deficient of Co centres is dependent on the degree of CoPc aggregation, highlighting a trade-off between loading weight and distribution of CoPc. Then, a 4% loading weight of CoPc on CNH(O) exhibited the optimal performance of H_2O_2 generation, achieving a H_2O_2 current density of 483 mA cm^{-2} at a potential of 0.3 V vs RHE with a Faradaic efficiency of 64%.

Introduction

The electrochemical method of reducing oxygen at cathode via a two-electron process (2e$^-$ORR) to produce hydrogen peroxide (H_2O_2) provides a more energy-saving and eco-friendly alternative compared to the traditional anthraquinone process.[1,2] Given the faster decomposition of H_2O_2 in electrolyte with high pH, electrosynthesis of H_2O_2 in neutral electrolyte allows a better control of the purity and yield. Moreover, decentralized electrosynthesis of H_2O_2 in neutral electrolyte is more suitable for applications in daily sanitation and hygiene management. Due to the difficulty in suppressing the competing 4e$^-$ORR to water, however, the catalytic performance currently experiences low activity of catalysts in 2e$^-$ORR and does not meet commercialization requirements.

The pioneer work on 2e$^-$ORR catalysts primarily focus on nonferrous metals and their alloys, such as Cu, Au, Pt, etc.[3–6] However, the high cost of nonferrous metal catalysts, combined with their low selectivity for 2e$^-$ORR processes under high overpotentials and current densities, hinders their large-scale application.[7] Molecular catalysts have been investigated in H_2O_2 electrosynthesis, due to the high activity and atomic utilization of nonferrous metal atoms.[8–11] In the framework of these molecular catalysts, the metal atom was normally immobilized by coordination organic ligands, it can serve as atomic active site for facilitating adsorption of oxygen in "end-on" configuration, which favors 2 electron route and results in an end product of H_2O_2.[12] Moreover, reasonable design of coordination structure is an effective method to modulate the electronic structure in the vicinity of metal site,[13,14] and optimizing the bonding energy with intermediates of *OOH, *O, and *OH for high activity of 2e$^-$ORR. Phthalocyanine as a prevalent organic molecular framework, can immobilize a range of metal atoms (Fe, Ni, Co and so on), among which cobalt phthalocyanine (CoPc) was predicted for high-rate 2e$^-$ORR. The theoretical calculations revealed that there was a decent interaction between the electron density of the Co center and the key *OOH intermediate that favored H_2O_2 electrosynthesis than other metal atoms.[15,16] However, the poor electronic conductivity of CoPc limits the catalytic performance of pure CoPc catalysts. Therefore, carbon-based materials were employed to support CoPc, which can effectively enhance electronic conductivity.[17] The stabilization of CoPc on carbon-based support was driven by π-π interaction, which can be tuned by the introducing of structural defects and changing strain on the carbon-based support.[18–20] Hence, the electronic structure of metal atom in molecular catalyst can be further tailoring by the modification of carbon-based support, thereby

[a] Y. Ding, Y. Guo
The Institute of Technological Sciences, School of Power and Mechanical Engineering,Wuhan University,
Wuhan 430072, Hubei, China
E-mail: yguo@whu.edu.cn

[b] Z. Xing
College of Physical Science and Technology,Central China Normal University,
Wuhan 430079, Hubei, China
E-mail: xingzhuo@ccnu.edu.cn

[c] C. Kuai, F. R. Wang
Materials and Catalysis Laboratory, Department of Chemical Engineering,University College London,
London WC1E 7JE, United Kingdom
E-mail: ryan.wang@ucl.ac.uk

Supporting information for this article is available on the WWW under https://doi.org/10.1002/celc.202400650

the interaction with intermediates of 2e⁻ORR, which provides an additional degree of freedom to control the activity of CoPc.

Here, we employed oxygen doped carbon nanohorns (CNH-(O)) as the support for loading CoPc by solvent-nonsolvent coating (denoted as CNH(O)-CoPc). The carbon nanohorns exhibit abundant structural defects and distortions that facilitate binding with oxygen functional groups, generating dipole-induced dispersion force with CoPc to strengthen the π-π interaction. Hence CNH(O) is a promising support for the even distribution and stabilization of CoPc, enabling the generation of active sites with an optimal electronic structure for high-rate 2e⁻ORR. We prepared a series of catalysts with various loading weights of CoPc and evaluated their catalytic performance using rotating ring-disk electrode (RRDE) and gas diffusion electrode (GDE) cell. Characterization revealed that CoPc tends to form catalyst aggregates during CoPc dispersion on the carbon-based support. X-ray photoelectron spectroscopy (XPS) and Raman spectra suggest that the active catalytic sites for 2e⁻ORR are the uniformly distributed CoPcs with electron-deficient Co center. However, the aggregation of CoPc significantly hinders the 2e⁻ORR for two main reasons. Firstly, the aggregates of CoPc facilitate adsorption of oxygen molecules in a "side-on" configuration on two adjacent Co centers, promoting the 4e⁻ORR by dissociating O–O bonds. Secondly, the aggregates of CoPc exhibit low electronic conductivity, which leads to poor electron transfer and the electronic isolation of active sites under applied potential. Then the active sites maintain a high valence state during the ORR, which is favorable for the 4e⁻ORR.[21] Consequently, there is a trade-off between the catalytic performance of 2e⁻ORR and the loading weight of CoPc. The moderate loading weight of CoPc dispersed on CNH(O) exhibits an outstanding catalytic performance, it can achieve a H_2O_2 current density of 483 mA cm^{-2} at low reduction potential (0.3 V vs Reversible Hydrogen Electrode (RHE)), while the Faradaic efficiency can maintain 64% in GDE cell. These results can provide valuable insights for the future design of molecular catalysts with stable and high efficiency in the H_2O_2 electrosynthesis.

Results and Discussion

Catalyst Preparation and Characterization

The support of CNH(O) was prepared by nitric acid (12 M) treatment of CNHs, which decreases the graphitic (sp^2-hybridized) carbon and oxidizes dangling bands with oxygen functional groups. These oxygen functional groups on CNH(O) enhance the π-π interaction with CoPc through dipole-induced dispersion force, which can improve the even distribution of CoPc with less aggregation.[15] Then the CoPc loading was conducted by solvent-nonsolvent method with CoPc and CNH-(O) dispersed DMF solution (Scheme 1). A prolonged acidification treatment on CNH(O) will lead to saturation of oxygen content, implying a limiting distribution of CoPc with high activity for 2e⁻ORR.[22] The loading weights of CoPc on CNH(O) at nominal percentages of 2%, 4%, and 6% are denoted as CNH(O)-x% CoPc (x = 2, 4 or 6). According to XPS data, these correspond to Co atom loadings of 0.25, 0.37, and 0.68 atom%, respectively. (Table S1).

The transmission electron microscope (TEM) image in Figure S1 shows that the CNH(O)s have a horn shape with a small conical degree, the average length is around 40 nm. These CNH(O)s aggregate into spherical clusters resembling dahlia with an average diameter of 35 nm. The unique morphology of CNH renders the tips susceptible to oxidation, thereby creating a favorable condition for the potential achievement of a discrete molecular distribution of CoPc on the tips of CNH(O).[23] The energy dispersive spectroscopy (EDS) mapping (Figure S2) indicates the oxygen is successfully introduced and uniformly doped on CNH(O). As shown in Figures 1a and b, the CNH(O)s did not exhibit significant changes in morphology after CoPc loading and maintained similar average lengths and diameters

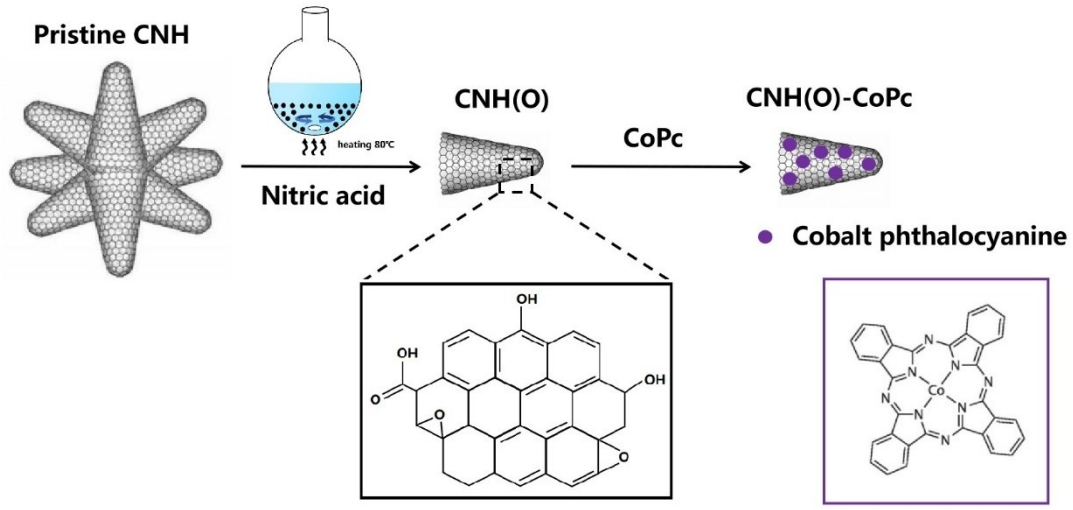

Scheme 1. Experimental schematic illustration of CNH acidification and CoPc loading.

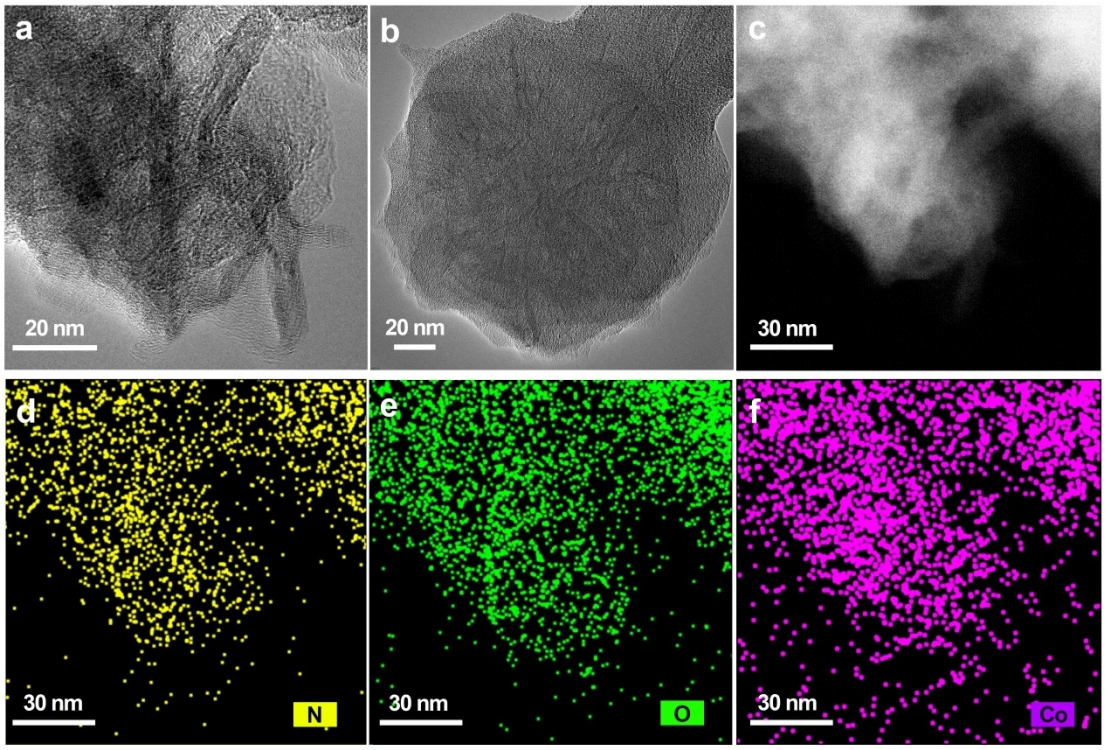

Figure 1. TEM images of CNH(O)-4% CoPc catalysts (a) and corresponding secondary spherical morphology (b), DF image (c) and N, O and Co EDS elemental mapping (d, e and f), respectively.

of spherical clusters compared to the prepared CNH(O). This is attributed to the physical method used for the distribution of CoPc. The dark-field (DF) images and corresponding EDS mapping of N, O, and Co elements in CNH(O)-4% CoPc are shown in Figure 1c-f respectively, indicating a uniform dispersion of CoPc on CNH(O), similar to that observed in CNH(O)-2% CoPc and -6% CoPc (Figure S3 and 4). While the different loading weight of CoPc on CNH(O) shows a different dense of CoPc distribution, suggesting that CoPc may form catalyst aggregates at large loading weight. The selected area electron diffraction (SAED) in Figure S5 exhibits a relatively sharp diffraction ring of (002) and (100), demonstrating a long-range network of sp^2-hybridized carbon atoms in CNH(O)-4% CoPc.

Although a uniform distribution of CoPc on CNH(O) at nano scale, the aggregation of CoPc during the GDE preparation appears to be inevitable. As shown in Figure S6–8, the scanning electron microscope (SEM) images of CNH(O)-x% CoPc reveal distinct rod-shaped crystals on the catalytic layer of GDE, which become more widespread with increasing loading weight of CoPc. These aggregates are the aggregation state of CoPc, as confirmed by EDS spot scanning analysis (Figure S7), consistent with evidence from other published works.[24,25] The X-ray diffraction (XRD) data for CNH(O) and CNH(O)-x% CoPc further confirm the aggregation of CoPc(Figure S9). CNH(O) exhibits typical carbon features, characterized by a prominent peak at (002) and two broad, inconspicuous peaks at (100) and (101), which align with the result from SAED of CNH(O)-4% CoPc. In contrast, the XRD pattern of CNH(O)-x% CoPc represents a hybrid phase of CNH(O) and CoPc, with the intensity of the characteristic peaks of CoPc increasing with higher CoPc loading weights. This occurs due to the planar structure of phthalocyanine molecules, which facilitates intermolecular aromatic ring stacking (π-π) interactions, leading to the formation of J-and/or H-aggregates.[26]

More structural insights of CNH(O)-CoPC were obtained from other spectroscopic characterizations. Firstly, we found that the Fourier transform infrared (FT-IR) spectroscopy of CNH(O)-CoPC (Figure 2a) was closely matched with the established CoPc spectra.[27] The vibrations of phthalocyanine are mainly distributed in the range of 400–1600 cm^{-1}. Additional bands attributable to CNH(O) can also be found at 1590 cm^{-1} and 1730 cm^{-1} when CoPc is hybridized with CNH(O). In addition, the Raman spectra of CNH(O)-CoPC with various loading weight of CoPc were compared. Based on the morphological features of the catalyst observed through SEM, the Raman spectroscopy results shown in Figure 2b were obtained from the area where CoPc uniformly dispersed and free of catalysts aggregates around. Clearly, these Raman spectra exhibit two obvious peaks at around 1580 and 1335 cm^{-1}, corresponding to the G peak associated with the high-frequency E_{2g} vibration and the D peak related to the defect-induced breathing modes of six atom rings in graphite basal plane. These G and D peaks are attributed to CNH(O)s, which are consistent with the Raman spectrum of original CNH(O)on GDE as shown in Figure S10a.[28] As appeared in the Raman spectra of CNH(O)-4% CoPc and -6% CoPc, distinct peaks at 675, 1130 and 1327 cm^{-1} correspond to the vibration of A_{1g} mode, peaks at 744 and 1525 cm^{-1} correspond to the

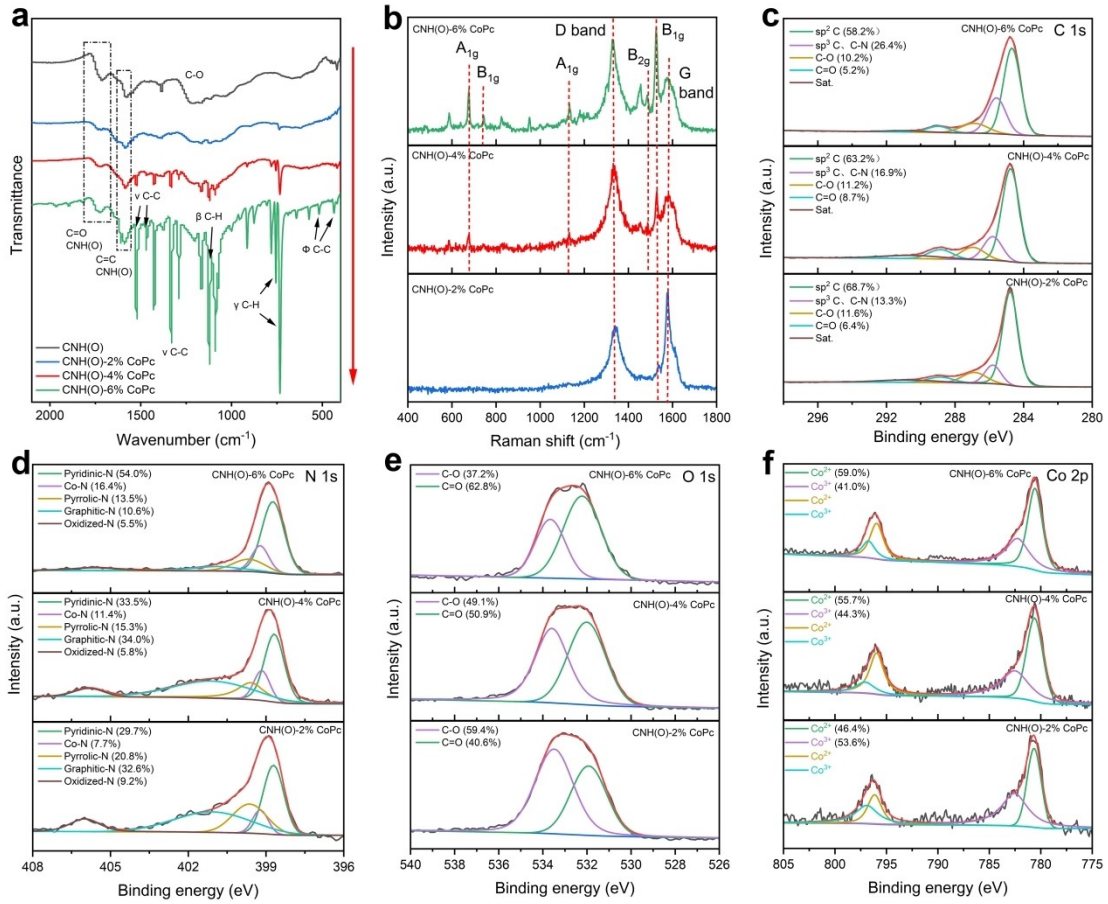

Figure 2. FT-IR spectra of CNH(O)-CoPc and pristine CNH(O) (a), Raman spectra of CNH(O) with various loading weight of CoPc (b), (c-f) XPS spectra of C1*s*, N1*s*, O1*s*, Co2*p* for the CNH(O) with various loading weight of CoPc, respectively. The red arrow in a represents the increase of CoPc loading. The proportion of Co^{3+} and Co^{2+} are only derived from the deconvolution of the peak of Co $2p_{3/2}$.

vibration of B_{1g} mode and 1485 cm^{-1} correspond to the vibration B_{2g} mode of CoPc, aligning with the Raman spectrum obtained from the CoPc aggregates (Figure S10b).[29] As loading weight of CoPc increases, the relative intensities of these peaks gradually increase, reflecting the rising degree of aggregation of CoPc. These FT-IR and Raman data collectively suggest that the molecular catalyst of CoPc on carbon-based support are susceptible to aggregation with increasing the loading weight. Moreover, the elemental composition and chemical states of the catalysts were examined by XPS as shown in Figure 2c-f and Figure S11–13. In the deconvoluted XPS spectra of C 1*s*, we attribute the increasing intensity at 285.8 eV to C–N bonds rather than sp^3 C. This observation is further supported by the increase in pyridinic N and Co–N bond proportions with larger CoPc loading weight, as shown in Figure 2d. Simultaneously, the XPS spectrum of O 1s reveals a decrease in the proportion of C–O bonds with increasing CoPc loading, suggesting that CoPc is preferentially stabilized by the oxygen functional groups associated with the C–O band. The Co 2p XPS spectrum shows two peaks around 781.0 eV and 796.3 eV, attributed to Co $2p_{3/2}$ and Co $2p_{1/2}$, respectively, as illustrated in Figure 2f. The binding energy shifts were evaluated through the deconvoluted peaks of Co^{2+} and Co^{3+} along with their relative proportions. In contrast to commercial CoPc powder (Figure S13), the CNH(O)-2% CoPc exhibits a higher proportion of Co^{3+}, indicating an electron-withdrawing effect from the oxygen functional groups on CNH(O), which results in an electron-deficient Co center. However, as the CoPc loading increases, the proportion of Co^{3+} in CNH(O)-6% CoPc approaches that of the commercial CoPc powder, suggesting an increase in the aggregation of CoPc with higher loading weights. These spectral changes suggest that the carbon support facilitates the distribution of CoPc through oxygen functional groups related to the C–O band, which in turn generates electron-deficient Co centers for the 2 e^-ORR. However, this distribution of CoPc is accompanied by the formation of aggregated catalysts at larger loading weight of CoPc.

ORR Performance Measurement

To evaluate the performance of the catalysts, ORR performance tests were conducted in RRDE and in situ GDE cell. First, we calibrated the H_2O_2 collection efficiency of RRDE by recording the linear sweep voltammetry (LSV) curves in an electrolyte of 10 mM $K_3Fe(CN)_6$ and 0.1 M Na_2SO_4 at the scan rate of

10 mV s^{-1}, which showed an apparent collection efficiency of 36.8%. Subsequently, the RRDE test was carried on in O_2-saturated 0.1 M Na_2SO_4 electrolyte at a rotation speed of 1600 rpm (Figure 3a). The results indicate that CNH(O)-4% CoPc exhibited the highest H_2O_2 (ring) current density among the catalysts with various loading weight of CoPc. Additionally, all catalysts with CoPc loading displayed positively shifted onset potentials compared to that on pristine CNH(O), indicating a lower reduction potential required for the 2e⁻ORR. The molar selectivity, Faradaic efficiency of H_2O_2 production and electron transfer number (*n*) of ORR, calculated from the corresponding LSV (Figure 3a), are presented in Figure 3b and S14. The selectivity of H_2O_2 on these catalysts decrease as the potential declines, indicating that ORR progressively shifts towards the 4-electron process at high reduction potentials and current densities in neutral electrolyte. Notably, the highest selectivity is achieved on CNH(O)-2% CoPc, while selectivity diminishes below that on pristine CNH(O) when the loading weight of CoPc exceeds 4%. This suggests that the aggregation of CoPc may alter the intrinsic activity of CNH(O)-x% CoPc, promoting the 4e⁻ORR pathway.

The catalytic performance was further assessed using a GDE cell, which facilitates the mass transfer process for high current density. The results of the LSV in Figure 3c demonstrate that CNH(O)s with CoPc loading achieve a larger current density compared to pristine CNH(O) under improved O_2 transfer. Among the samples tested, CNH(O)-4% CoPc exhibits the largest current density, consistent with their performance in RRDE. Specifically, the chronoamperometry with iR compensation for the catalysts at 0.3 V versus RHE were presented in Figure 3d. The current density exhibits a gradual increase after an activation period, indicating that gas/electrolyte balance has been achieved within the catalyst layer on the GDE. The partial current density of H_2O_2 and the Faradaic efficiency of these catalysts, measured by titration, are plotted in Figure 3e and f respectively. Notably, the current density of H_2O_2 initially

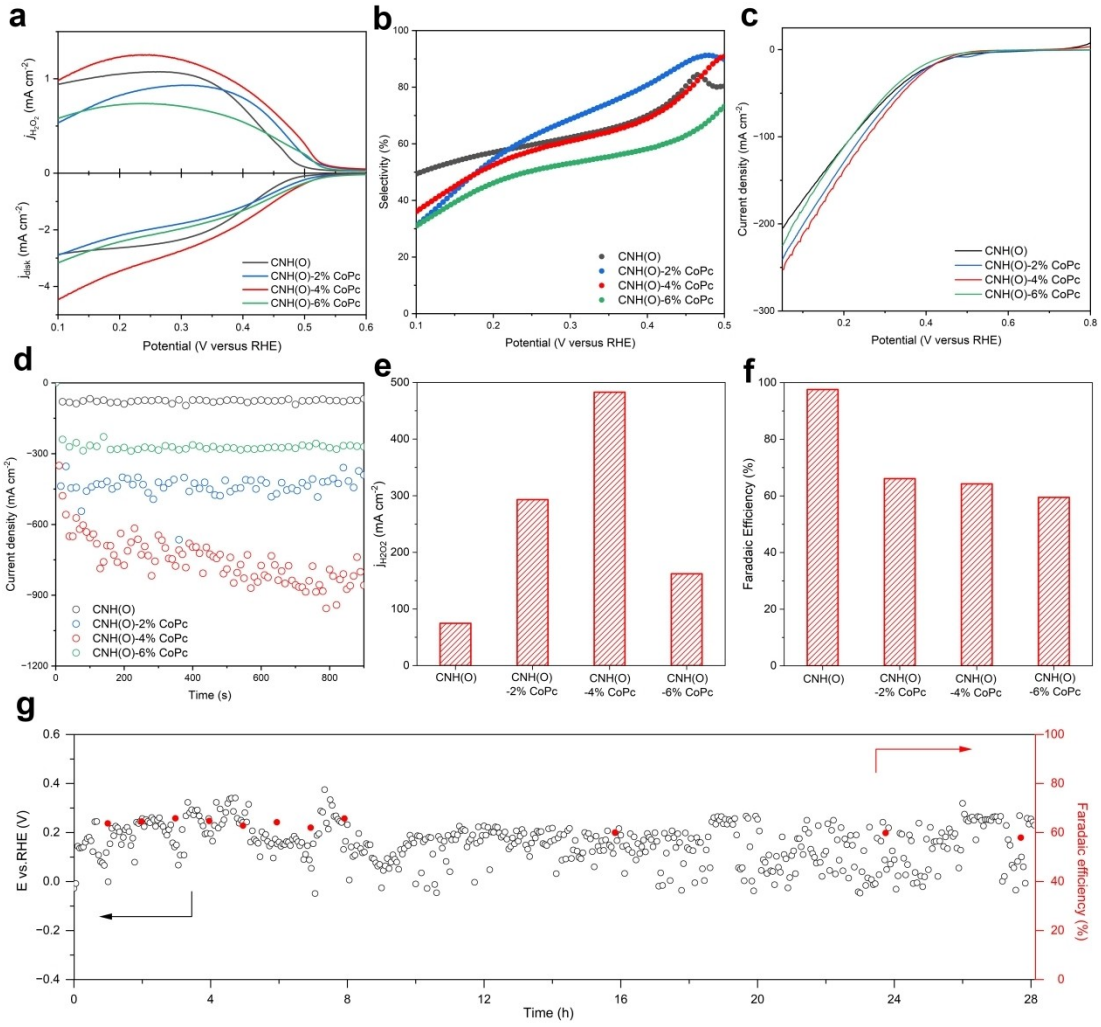

Figure 3. (a) LSV curves of CNH(O) with various loading weight of CoPc and pristine CNH(O) on the RRDE (1600 rpm) at a scan rate of 10 mV s^{-1} in O_2—saturated 0.1 M Na_2SO_4 electrolyte, together with the H_2O_2 currents detected on the Pt ring electrode (upper panel) at 1.20 V vs RHE. (b) Corresponding molar selectivity for H_2O_2 production. (c) LSV curves of CNH(O) with various loading weight of CoPc and pristine CNH(O) in GDE-cell. (d) chronoamperometry, (e) H_2O_2 current density and (f) Faradaic efficiency of CNH(O) with various loading weight of CoPc and pristine CNH(O) at 0.3 V versus RHE in GDE-cell. (g) the chronopotentiometry test for catalyst CNH(O)-4% CoPc in GDE-cell at 200 mA cm^{-2}.

increases and then decreases with increasing loading weight of CoPc on CNH(O), reaching the apex at CNH(O)-4% CoPc. Although the Faradaic efficiencies on CNH(O)-CoPc are lower than that on pristine CNH(O), decreasing from 66% on CNH(O)-2% CoPc to 60% on CNH(O)-6% CoPc, the H_2O_2 current density of CNH(O)-4% CoPc can achieve 483 mA cm^{-2} with Faradaic efficiency of 64%. This performance is remarkable for the electrosynthesis of H_2O_2 in neutral electrolyte and surpasses that of the majority of state-of-the-art electrocatalysts.[30–32] To evaluate the stability of CNH(O)-4% CoPc, a chronopotentiometry test was conducted in GDE-cell at 200 mA cm^{-2}. As shown in Figure 3g, the catalyst exhibits stable Faradaic efficiencies of approximately 62% over a lifetime exceeding 28 hours. However, the flooding issue of GDE results in a slight decrease in Faradaic efficiency to 57.8%. This result demonstrates a decent stability of the CNH(O)-x% CoPc on GDE, indicating significant potential for practical application.

Based on the experiment results described, we infer that the convex relationship between the H_2O_2 current density of CNH(O) and the loading weight of CoPc represents a trade-off between the uniform distribution and aggregation of CoPc. The presence of oxygen functional groups with C–O bonds in CNH(O), including C–O–C in furans, esters, anhydrides, and C–OH in phenolic and carboxylic groups, facilitates the immobilization of CoPc, as evidenced by XPS data. These oxygen functional groups modulate the electron structure at the Co center, rendering electron delocalization of Co due to stronger dipole interactions. This is reflected in the deconvolution of high-valance Co^{3+} observed in the XPS spectra of Co 2p. The electron-deficient Co center results in a downshifted d-band center, which optimizes the adsorption energy of the key intermediate *OOH to a more favorable state, thereby facilitating the electrosynthesis of H_2O_2 at high current densities.[33] Due to the intermolecular π-π interaction, it is challenging to prevent the aggregation of CoPc on carbon-based support. However, the aggregates of CoPc not only exhibit a low electronic conductivity,[34] but also promote "side-on" adsorption of O_2.[35] This phenomenon hinders the electron delivery to the active sites,[36] thereby impending the *OOH reduction to *O and H_2O.[37] Consequently, this suggests that the increasing CoPc loading does not result in a stoichiometric increase in the number of active sites, rather leads to the concomitant forming of CoPc aggregates that facilitate the 4e$^-$ORR. Since aggregation is common in metal molecular catalysts with a similar framework to CoPc, the results suggest the need for a reasonable approach to the deposition of molecular catalysts on carbon supports.

Conclusion

In conclusion, we employed oxygen-doped carbon nanohorns (CNH(O)) to support CoPc for the electrosynthesis of H_2O_2. The CNH(O) structures possess abundant defects that enhance the interaction with CoPc molecules, promoting uniform distribution and altering the electronic structure of the Co center as active sites. However, due to unsuppressed aggregation, there exists a trade-off between the activity of H_2O_2 electrosynthesis and CoPc loading on CNH(O). Notably, CNH(O)-4% CoPc achieves the highest catalytic performance, demonstrating an H_2O_2 current density of 483 mA cm^{-2} and a Faradaic efficiency of 64% at the potential of 0.3 V vs. RHE. This result underscores the critical role of carbon support in achieving uniform distribution of CoPc and highlights how the aggregation of molecular catalysts affects catalytic performance. Furthermore, it suggests the necessity for a rational approach to catalyst preparation in future catalyst design.

Experimental Section

Reagents and Materials

$KMnO_4$, $K_3[Fe(CN_6)]$, ethanol, isopropanol, nitric acid (65–68%), sodium sulfate (Na_2SO_4, 99.98%) were purchased from Sinopharm Chemical Reagent Co., Ltd, Graphite rod were purchased from ADHST. AvCarb GDS2230 substrates and Nafion 1110 membranes were purchased from Sci Materials hub. Nafion perfluorinated resin solution (5 wt%) was purchased from Sigma-Aldrich. Leak-free Ag/AgCl reference electrodes (Model LF-1) were purchased from Innovative Instruments. O_2 (99.999%) gas was purchased from NRD. Deionized water with a specific resistance of 18.2 MΩ·cm was used throughout the experiments.

Preparation of Molecular Electrocatalysts

Synthesis of molecular electrocatalysts followed a two-step procedure.

(1) **Preparation of O-doped carbon nanohorns.** Typically, 100 mg of CNH was dispersed in 100 mL of 12.0 M nitric acid solution. The suspension was then refluxed at 80 °C for 24 h to obtain O-doped carbon nanohorns (CNH(O)). After cooling down overnight, the slurry was collected after centrifugation and washed with DI water until the pH was neutral. Finally, the carbon materials were dried at 80 °C in oven overnight.

(2) **CoPc dispersed on the CNH(O) surface.** Briefly, 30 mg of CNH(O) was added to 20 ml DMF solution, which is referred to as solution 1. Meanwhile, a calculated amount of CoPc (2, 4, 6 wt%, nominal loading weight) was added to another DMF solution (20 ml), referred to as solution 2. Both solutions 1 and 2 were then sonicated for at least 30 min to disperse CNH(O) and CoPc in the DMF solution. Solution 2 was then added to solution 1 and the mixture was sonicated for at least 30 min. The obtained mixture was vigorously stirred for 24 hours at room temperature, then washed by centrifugation three times with DMF, ethanol, and water, respectively, and finally redispersed in water. Final molecular electrocatalysts were obtained by freeze-drying the mixture solution.

Material Characterization

TEM images and EDS mapping were acquired using a JEM-F200 transmission electron microscope with a field emission gun operated at 200 kV. SEM images were acquired using a ZEISS GeminiSEM 500 scanning electron microscope. Raman spectra were acquired using LabRAM HR Evolution Micro-Raman Spectrometer. XPS data were acquired using a Thermo Scientific ESCALAB XI$^+$ X-ray Photoelectron Spectrometer with an Al Kα X-ray source (1486.67 eV). IR spectra were acquired using a NICOLET FTIR 5700 Spectrometer.

Electrochemical Measurements

The electrochemical measurements were initially conducted using a conventional three-electrode cell configuration with a rotating ring-disk electrode (RRDE) system. Typically, 3.3 mg of prepared CNH(O) was mixed with 1 mL of isopropanol and 10 μL of Nafion solution (5 wt%) to form a homogeneous catalyst ink after 20 min ultrasonication. 6 μL of the catalyst ink was carefully pipetted onto a glassy carbon disk (0.196 cm^2 area) to form a uniform catalyst layer with a mass loading of 0.10 mg cm^{-2}, which was then dried at 60 °C in an oven. The measurements were performed using a CHI 760E Bipotentiostat and a Pine Modulated Speed Rotator with CE Mark at room temperature. A RRDE assembly (Gaossunion) consisting of a glassy carbon rotation disk electrode (Φ = 5.0 mm) and a Pt ring (Φ = 8.0 mm) was used, which has a theoretical collection efficiency of 37%. Experimentally, the apparent collection efficiency (N) was determined to be 36.8% in the ferrocyanide/ferricyanide half reaction system at a rotation speed between 400 and 2000 rpm. ORR was tested in O_2-saturated 0.1 M Na_2SO_4 electrolyte with a fixed rotation speed of 1600 rpm, and a potential of 1.20 V vs RHE was applied on the Pt ring electrode to collect the generated H_2O_2. A Ag/AgCl electrode was used as the reference electrode. All potentials measured against the Ag/AgCl electrode were converted to the RHE scale in this work: E(vs RHE) = E(vs Ag/AgCl) + 0.197 V + 0.0591×pH. The electron-transfer number (n) and molar selectivity of H_2O_2 (fraction of O_2 used for producing H_2O_2) was determined from the disk current for O_2 reduction and the Pt ring current for H_2O_2 oxidation, as shown in the following equation:[38]

$$n = \frac{i_d}{i_d + \frac{i_r}{N}} \times 4$$

$$\text{Molar selectivity of } H_2O_2 = \frac{\frac{i_r}{N}}{i_d + \frac{i_r}{N}} \times 200\,\%$$

The Faradaic efficiency for H_2O_2 production can be calculated using equation:

$$\text{Faradaic efficiency of } H_2O_2 = \frac{\frac{i_r}{N}}{i_d} \times 100\,\%$$

where i_d is the current on the disk electrode, i_r is the current on the Pt ring electrode, and N is the calibrated collection efficiency (36.8%).

To quantify the amount of generated H_2O_2 molecules and achieve high current density of industrial level, we firstly performed electrosynthesis in GDE flow cell. To prepare the ink, 2 mg of CNH(O) powder and 2 mg pure carbon powder were dispersed in 1 mL of isopropanol each. After sonication for 0.5 h, the two dispersions were mixed together, then 20 μL of Nafion solution (5 wt%) was added and sonicated for another 0.5 h, which was used as catalyst ink. The catalyst ink was sprayed on an AvCarb GDS2230 substrate with a mass loading of 0.5 ± 0.20 mg cm^{-2} by air brush, which was then dried at room temperature. Electrochemical measurements were performed using a Gamry Interface 1000 Potentiostat and a home-built GDE flow cell.[39] The GDE flow cell consists of a Ti current collector with interdigitated gas-diffusion channels, a cathodic GDE with catalyst layer deposited on AvCarb GDS2230 substrate, a 3D-printed chamber with ports for electrolyte flow and reference electrode, and an commercial IrO_2 deposited Ti foam inserted in a pocket of Ti current collector as the anode. The gas-diffusion channels have a depth of 0.2 mm and a density of 50 channels cm^{-1}. The above prepared electrodes were used as working electrodes with an effective area of 0.66 cm^2, and a leak-free Ag/AgCl electrode was used as the reference electrode. The cathode and anode chambers were separated by a piece of Nafion 1110 membrane. The catholyte and the anolyte were each 20 mL of 1 M Na_2SO_4 solution circulated using peristaltic pumps at a flow rate of 2.0 mL min^{-1}, and the O_2 gas flow was controlled by mass flow controller (Yidu, PIPG-S101-01-0020). All potentials were iR-compensated and converted to the RHE scale in the GDE-cell tests. The reported current densities for H_2O_2 production were normalized to geometric surface areas. The concentration of H_2O_2 in the electrolyte was estimated by titration with $KMnO_4$. For titration with $KMnO_4$, 1 mL of the post-electrolysis catholyte was mixed with 2 mL of 20% H_2SO_4, and then titrated by 20 mM of $KMnO_4$ based on the following equation:

$$H_2O_2 + 2KMnO_4 + 3H_2SO_4 \rightarrow 5O_2 + 2MnSO_4 + K_2SO_4 + 8H_2O$$

The Faradaic efficiency for H_2O_2 production was calculated using the following equation:

$$\text{Faradaic efficiency of } H_2O_2 = \frac{C_{H2O2} \times V \times 2 \times 96485}{Q_{total}} \times 100\%$$

Where C_{H2O2} is the measured concentration of H_2O_2, V is the volume of the catholyte, Q_{total} is the total quantity of electric charge for the electrolysis.

Acknowledgements

This work was financially supported by the NSFC (no. U2241244 and 12275199) of China, EPSRC (EP/S018204/2, EP/Z001730/1 and EP/Y036220/1), Guangdong Basic and Applied Basic Research Foundation (no. 2024A1515010383 and 2022A1515110149) and Shandong Provincial Natural Science Foundation (ZR2020QB133).

Conflict of Interests

The authors declare no conflict of interest.

Keywords: Carbon nanohorns · Molecular catalysts · Cobalt phthalocyanine · Electrochemistry oxygen reduction · Hydrogen peroxide

[1] K. Dong, Z. Xu, X. He, D. Zhao, H. Chen, J. Liang, Y. Luo, S. Sun, D. Zheng, Q. Liu, A. A. Alshehri, Z. Feng, Y. Wang, X. Sun, *Chem. Commun.* **2022**, *58*, 10683–10686.
[2] Y. Yao, H. Wang, K. Dong, H. Li, J. Liang, R. Li, S. Sun, Z. Cai, X. He, D. Zheng, Y. Luo, S. Alfaifi, D. Ma, W. Hu, X. Sun, *J. Mater. Chem. A* **2023**, *11*, 22154–22160.
[3] X. Shi, S. Siahrostami, G. L. Li, Y. Zhang, P. Chakthranont, F. Studt, T. F. Jaramillo, X. Zheng, J. K. Norskov, *Nat. Commun.* **2017**, *8*, 701.
[4] F. Li, Q. Shao, M. Hu, Y. Chen, X. Huang, *ACS Catal.* **2018**, *8*, 3418–3423.
[5] H. Xu, D. Cheng, Y. Gao, *ACS Catal.* **2017**, *7*, 2164–2170.
[6] K. Kisand, A. Sarapuu, A. L. Peikolainen, H. Seemen, M. Kook, M. Käärik, J. Leis, V. Sammelselg, K. Tammeveski, *ChemElectroChem* **2018**, *5*, 2002–2009.
[7] C. M. Sanchez-Sanchez, A. J. Bard, *Anal. Chem.* **2009**, *81*, 8094–8100.
[8] Z. Li, R. Wu, S. Xiao, Y. Yang, L. Lai, J. S. Chen, Y. Chen, *Chem. Eng. J.* **2022**, *430*, 132882.

[9] M. Li, H. Wang, W. Luo, P. C. Sherrell, J. Chen, J. Yang, *Adv. Mater.* **2020**, *32*, 2001848.
[10] T. Tang, Z. Wang, J. Guan, *Adv. Funct. Mater.* **2022**, *32*, 2218–2223.
[11] H. Cheng, X. Wu, X. Li, X. Nie, S. Fan, M. Feng, Z. Fan, M. Tan, Y. Chen, G. He, *Chem. Eng. J.* **2021**, *407*, 126842.
[12] L. Lin, N. Miao, G. G. Wallace, J. Chen, D. A. Allwood, *Adv. Energy Mater.* **2021**, *11*, 2100695.
[13] Y. Kumar, E. Kibena-Põldsepp, J. Kozlova, A. Kikas, M. Käärik, J. Aruväli, V. Kisand, J. Leis, A. Tamm, K. Tammeveski, *ChemElectroChem* **2021**, *8*, 2662–2670.
[14] L. Zong, M. Li, P. Li, K. Fan, L. Wang, *Angew. Chem. Int. Ed.* **2024**, *64*, e202413933.
[15] B.-H. Lee, H. Shin, A. S. Rasouli, H. Choubisa, P. Ou, R. Dorakhan, I. Grigioni, G. Lee, E. Shirzadi, R. K. Miao, J. Wicks, S. Park, H. S. Lee, J. Zhang, Y. Chen, Z. Chen, D. Sinton, T. Hyeon, Y.-E. Sung, E. H. Sargent, *Nat. Catal.* **2023**, *6*, 234–243.
[16] P. Cao, X. Quan, X. Nie, K. Zhao, Y. Liu, S. Chen, H. Yu, J. G. Chen, *Nat. Commun.* **2023**, *14*, 172.
[17] K. Dong, J. Liang, Y. Ren, Y. Wang, Z. Xu, L. Yue, T. Li, Q. Liu, Y. Luo, Y. Liu, S. Gao, M. S. Hamdy, Q. Li, D. Ma, X. Sun, *J. Mater. Chem. A* **2021**, *9*, 26019–26027.
[18] J. Choi, P. Wagner, S. Gambhir, R. Jalili, D. R. MacFarlane, G. G. Wallace, D. L. Officer, *ACS Energy Lett.* **2019**, *4*, 666–672.
[19] X. Kong, G. Liu, S. Tian, S. Bu, Q. Gao, B. Liu, C. S. Lee, P. Wang, W. Zhang, *Small* **2022**, *18*, 2204615.
[20] X. Zhang, Z. Wu, X. Zhang, L. Li, Y. Li, H. Xu, X. Li, X. Yu, Z. Zhang, Y. Liang, H. Wang, *Nat. Commun.* **2017**, *8*, 14675.
[21] S. Ren, E. W. Lees, C. Hunt, A. Jewlal, Y. Kim, Z. Zhang, B. A. W. Mowbray, A. G. Fink, L. Melo, E. R. Grant, C. P. Berlinguette, *J. Am. Chem. Soc.* **2023**, *145*, 4414–4420.
[22] Z. Xing, K. Shi, Z. S. Parsons, X. Feng, *ACS Catal.* **2023**, *13*, 2780–2789.
[23] N. Karousis, I. Suarez-Martinez, C. P. Ewels, N. Tagmatarchis, *Chem. Rev.* **2016**, *116*, 4850–4883.
[24] X. Wu, J. W. Sun, P. F. Liu, J. Y. Zhao, Y. Liu, L. Guo, S. Dai, H. G. Yang, H. Zhao, *Adv. Funct. Mater.* **2022**, *32*, 2107301.
[25] W. S. Dean, T. L. Soucy, K. E. Rivera-Cruz, L. L. Filien, B. D. Terry, C. C. L. McCrory, *Small* **2024**, 2402293.
[26] C. A. Hunter, J. K. M. Sanders, *J. Am. Chem. Soc.* **1990**, *112*, 5525–5534.
[27] N. Han, Y. Wang, L. Ma, J. Wen, J. Li, H. Zheng, K. Nie, X. Wang, F. Zhao, Y. Li, J. Fan, J. Zhong, T. Wu, D. J. Miller, J. Lu, S.-T. Lee, Y. Li, *Chem.* **2017**, *3*, 652–664.
[28] A. C. Ferrari, D. M. Basko, *Nat. Nanotechnol.* **2013**, *8*, 235–246.
[29] M. Szybowicz, W. Bała, K. Fabisiak, K. Paprocki, M. Drozdowski, *Cryst. Res. Technol.* **2010**, *45*, 1265–1271.
[30] L. Jing, W. Wang, Q. Tian, Y. Kong, X. Ye, H. Yang, Q. Hu, C. He, *Angew. Chem. Int. Ed.* **2024**, *63*, e202403023.
[31] L. Jing, Q. Tian, W. Wang, X. Li, Q. Hu, H. Yang, C. He, *Adv. Energy Mater.* **2024**, *14*, 2304418.
[32] Y. Zhang, M. Wang, W. Zhu, M. Fang, M. Ma, F. Liao, H. Yang, T. Cheng, C. W. Pao, Y. C. Chang, Z. Hu, Q. Shao, M. Shao, Z. Kang, *Angew. Chem. Int. Ed.* **2023**, *62*, e202218924.
[33] H. Jin, P. Li, P. Cui, J. Shi, W. Zhou, X. Yu, W. Song, C. Cao, *Nat. Commun.* **2022**, *13*, 723.
[34] M. Zhu, R. Ye, K. Jin, N. Lazouski, K. Manthiram, *ACS Energy Lett.* **2018**, *3*, 1381–1386.
[35] Y. Zhu, Y. Jiang, H. Li, D. Zhang, L. Tao, X. Z. Fu, M. Liu, S. Wang, *Angew. Chem. Int. Ed.* **2024**, *63*, e202319370.
[36] N. Corbin, J. Zeng, K. Williams, K. Manthiram, *Nano Res.* **2019**, *12*, 2093–2125.
[37] S. Siahrostami, S. J. Villegas, A. H. Bagherzadeh Mostaghimi, S. Back, A. B. Farimani, H. Wang, K. A. Persson, J. Montoya, *ACS Catal.* **2020**, *10*, 7495–7511.
[38] C. Xia, J. Y. Kim, H. Wang, *Nat. Catal.* **2020**, *3*, 605–607.
[39] Z. Xing, L. Hu, D. S. Ripatti, X. Hu, X. Feng, *Nat. Commun.* **2021**, *12*, 136.

Manuscript received: December 4, 2024
Revised manuscript received: January 22, 2025
Version of record online: February 7, 2025